HOKKAIDO UNIVERSITY

Title	Observation of surface seismic activity changes of an Alpine glacier during a glacier-dammed lake outburst
Author(s)	Roux, P.-F.; Walter, F.; Riesen, P. et al.
Citation	Journal of Geophysical Research, Earth Surface, 115, F03014 https://doi.org/10.1029/2009JF001535
Issue Date	2010-07-31
Doc URL	https://hdl.handle.net/2115/48771
Rights	Copyright 2010 by the American Geophysical Union.
Type	journal article
File Information	JGR115_F03014.pdf

Hokkaido University Collection of Scholarly and Academic Papers : HUSCAP

JOURNAL OF GEOPHYSICAL RESEARCH, VOL. 115, F03014, doi:10.1029/2009JF001535, 2010

Click Here for Full Article

Observation of surface seismic activity changes of an Alpine glacier during a glacier-dammed lake outburst

P.-F. Roux,[1] F. Walter,[2] P. Riesen,[2] S. Sugiyama,[2,3] and M. Funk[2]

Received 18 September 2009; revised 5 February 2010; accepted 23 February 2010; published 31 July 2010.

[1] During the 2004 outburst flood of Gornersee, Switzerland, we observed surface microseismic activity (so-called icequakes) near the glacier-dammed lake on Gornergletscher. Using surface waves, we located near-surface tensile fracturing events by inverting time delays using a quasi-Newton scheme. We located 8520 near-surface events with uncertainties of less than 10 m. Seismic activity increased during the lake drainage, and the icequake epicenters migrated downglacier. Furthermore, we identified events whose fault plane orientations are nearly perpendicular to the local pattern of surface crevassing. These observations can be explained by the rotation of principal strains at the glacier surface deduced from local ice flow measurement which occurred during the flotation of the ice dam at the onset of the lake drainage. In general, we suggest that our technique is a useful tool to locate large data sets of microseismic events and can be used to monitor the temporal evolution of fracture processes and their dependence on glacier flow and glacier hydrology.

Citation: Roux, P.-F., F. Walter, P. Riesen, S. Sugiyama, and M. Funk (2010), Observation of surface seismic activity changes of an Alpine glacier during a glacier-dammed lake outburst, *J. Geophys. Res.*, *115*, F03014, doi:10.1029/2009JF001535.

1. Introduction

[2] Glaciers are known to be the source of seismic energy recorded by seismometers as so-called icequakes. Several past studies have shown icequakes to exhibit a wide variety in their sources and physical origins, ranging from surface events linked to crevassing processes [*Neave and Savage*, 1970] to deep seated sources related to the friction of the ice over the bedrock [e.g., *Danesi et al.*, 2007; *Roux et al.*, 2008] or to internal hydrological processes [*St. Lawrence and Qamar*, 1979]. Recently, *Walter et al.* [2008] studied the outburst flood of a glacier-dammed lake (also known as a "jökulhlaup" [see *Roberts*, 2005]) and possible hydrofracturing occurring at the base. *Walter et al.* [2008] showed evidence for a correlation between water level variations and the occurrence of deep events, further proving the link between subglacial water pressure and seismic activity. Jökulhlaups represent a severe threat in many mountain ranges and are known to have caused major destruction [e.g., *Raymond et al.*, 2003]. This underlines the need to better understand their onset and behavior. As glacier flow can be strongly perturbed by an outburst flood [*Björnsson*, 1998; *Roberts*, 2005], studies of the latter provide the opportunity to investigate the relation between changing subglacial conditions and glacier dynamics.

[3] In the present paper, we analyze the influence of such an outburst event on the surface seismic activity of an alpine glacier. We focus on Gornergletscher, a 14 km long polythermal Alpine valley glacier located close to the Monte Rosa massif in southern Switzerland (Figure 1). At an elevation of approximately 2500 m it merges with another tributary called Grenzgletscher (Figure 1). In the confluence, an ice marginal lake (known as Gornersee) (Figure 1) forms every year at the beginning of spring and drains (usually subglacially) in the following summer [*Huss et al.*, 2007].

[4] During summer 2004, investigators from ETH Zürich installed a network of seismometers in order to measure seismic activity associated with the outburst of Gornersee [*Walter et al.*, 2008]. We have developed a technique, described here, for automatically and efficiently locating the seismic epicenters. Although sources at depth (i.e., between the depth of crevasse penetration and the underlying bedrock) exist [*Deichmann et al.*, 2000; *Walter et al.*, 2008], most of the recorded seismicity is generated by shallow sources, generally no deeper than a few meters, such as crevassing [e.g., *Neave and Savage*, 1970]. Such shallow sources can be regarded as indicative of the mean state of stress within the ice mass, and in particular of failure strain of the ice. Measuring the seismic activity related to these surface processes therefore gives a means to characterize dramatic changes in the stress field leading to brittle deformation of the glacier. *Roberts* [2005] has inferred the occurrence of strong modifications to the stress field during outburst flood events; in the present paper, we propose to examine any such changes during a Gornersee outburst event using its seismological signature.

2. Overview of the Outburst

[5] Here we give a brief description of the 2004 outburst event, which has been extensively described and analyzed by

[1]Laboratoire de Géophysique Interne et Tectonophysique, Université de Savoie, CNRS, Le Bourget-du-Lac, France.
[2]Versuchsanstalt für Wasserbau, Hydrologie und Glaziologie, ETH Zurich, Zurich, Switzerland.
[3]Institute of Low Temperature Science, Hokkaido University, Sapporo, Japan.

Copyright 2010 by the American Geophysical Union.
0148-0227/10/2009JF001535

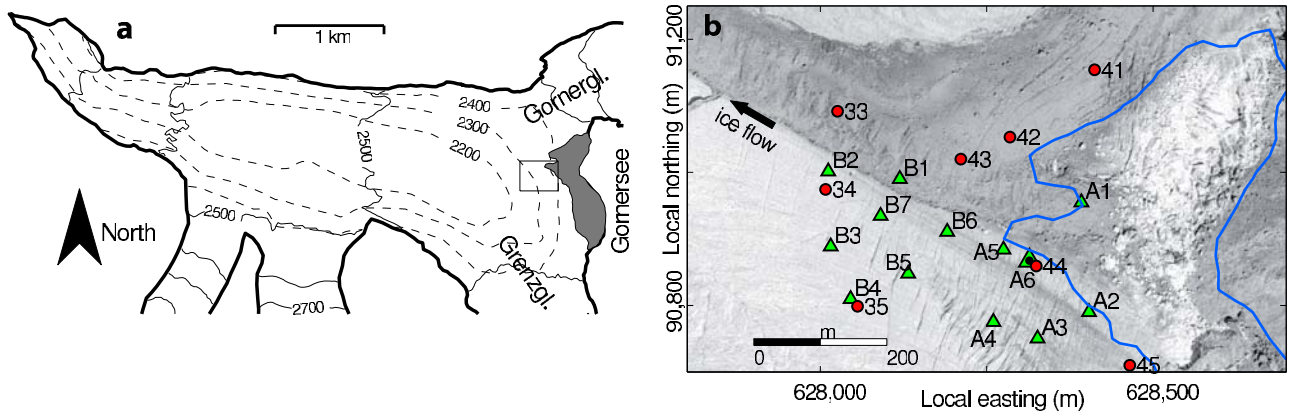

Figure 1. (a) Map of tongue of Gornergletscher showing both Gornersee (gray area) and the location of the seismic network (box near the lake). Solid and dashed contour lines approximate the glacier surface and the glacier bed, respectively. Also shown is the tributary called Grenzgletscher visible on the southeastern part of the map. (b) Orthophotograph showing the study site. Seismometers are represented as green triangles, and stakes are shown as red dots. Two seismometers were installed at the location of the large dotted triangle, including at the ice surface and in a 100 m deep borehole. The outline of Gornersee at its maximum level is indicated by the blue line. The photograph was taken after the lake drainage. Coordinates are given in the Swiss Grid. The darker upper portion of the orthophotograph shows medial moraine debris.

Sugiyama et al. [2007], *Huss et al.* [2007], and *Sugiyama et al.* [2008]. According to *Huss et al.* [2007], the lake began to form in mid-May and reached an amount of stored water prior to the outburst of $\approx 4 \times 10^6$ m^3. The jökulhlaup can be separated into three main events. First, the lake water overtopped the ice dam on 1 July, prior to the main drainage phase. Second, on the same day, about 2% of the total amount of stored lake water was transferred into subglacial space. This resulted in a sudden decrease of about 30 cm of the lake level. The lake level kept on rising until the outburst began on 2 July. Then the level began to decrease gradually, and the subsequent calving of marginal ice at the north of the lake increased the discharge rate. Postoutburst examination of the lake showed that the drainage occurred via a combination of subglacial and englacial drainage [*Sugiyama et al.*, 2008]. The outburst began on 2 July and ended on 7 July.

3. Field Measurements

3.1. Measuring the Seismic Activity

[6] The seismic network was composed of two Geometrics GEODE seismic recorders connected to 13 three-component, 1 Hz seismometers (Lennartz LE-3D) and to a 28 Hz borehole seismometer (Geospace GS-20DH) installed at 100 m depth. The array layout is shown in Figure 1 along with stake positions (pictured as red dots). In order to employ a two-dimensional and instrumentally uniform array, we did not use the borehole sensor in the analysis. The resulting array aperture (i.e., maximum interstation distance, d_{max}) is $\approx$445 m and interstation distance d_{min} of neighboring stations is $\approx$50 m.

[7] The seismic signal was acquired at a sampling frequency of 1000 Hz in trigger mode using a short-term average/long-term average [*Allen*, 1978] method with STA and LTA window lengths of 80 ms and 800 ms, respectively. The trigger threshold ratio was set to 10. If the trigger condition was satisfied at four or more stations, the ground velocity was recorded for 2 s (including a 0.5 s pretrigger time window). In total, approximately 35000 events were detected during the 2004 field campaign (Figure 2). Note that seismic recordings stopped on 6 July although the outburst ended on 7 July. Further details upon the seismic instrumentation and parameters used in this field campaign are given by *Walter et al.* [2008].

[8] In order to separate the seismic activity recorded before the drainage from that recorded after the drainage, we look for transition times between different rates of seismic activity (Figure 2b). To do so, we search the best piecewise linear approximation to the cumulative counts with an unknown number of segments, therefore assuming constant seismic rates. As a consequence, we invert for a variable number of unknowns related together by the following equation:

$$N = r_i(t - t_{i-1}) + t_{i-1}, \; i \in [[1, n]] \tag{1}$$

where N is the cumulative number of events at time t, n is the number of segments, r_i is the seismic rate for segment i and t_i is the transition time between two consecutive segments. t_i further satisfies the condition $t_0 = 0$. We perform a grid search over these parameters, limiting the number of segments n to a maximum value of 3, and find the results shown in Figure 2b. In particular, we interpret the large change in slope on 2 July as the outburst flood initiation, which is consistent with field observations [e.g., *Huss et al.*, 2007; *Sugiyama et al.*, 2008].

3.2. Ice Flow and Deformation Measurements

[9] The three-dimensional ice flow of Gornergletscher was measured using either differential GPS or an automated theodolite. Both the GPS reference station and the theodolite were located on the bedrock at the northern flank of the glacier. Stakes were installed in the glacier surface (at locations identified by red dots in Figure 1) and were equipped with reflectors (stakes 33–35, 41 and 43–45 in Figure 1) or GPS receivers (stake 42 in Figure 1). The automated theodolite was operated on an hourly basis while the GPS receivers recorded the L1 and L2 phase signals on a three hourly basis

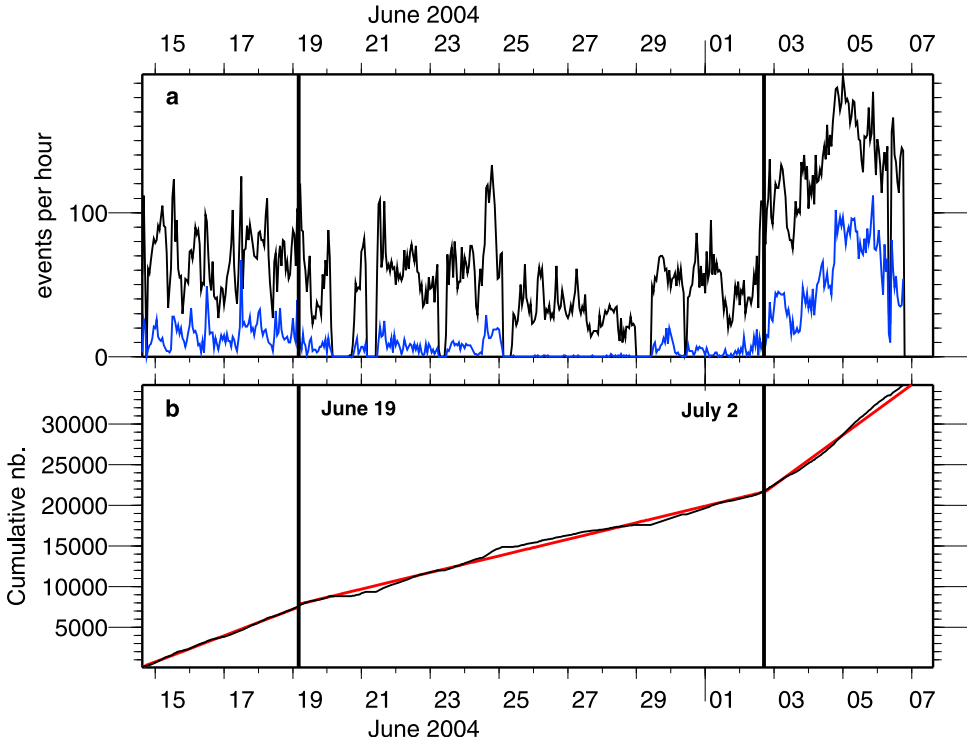

Figure 2. (a) Seismic activity expressed in number of events per hour. The entire data set (i.e., both located and not located events) is shown in black while the blue curve corresponds to the located events only. (b) Cumulative number of icequakes (black line) with the three corresponding best fitting linear regimes (red line). The transition times are indicated by the vertical bold black lines (see text for details).

for static epochs of 1 h. *Sugiyama et al.* [2008] give a detailed description of both systems. All in all, *Sugiyama et al.* [2008] report positional errors up to 10 millimeters and about 3 to 5 mm on the automated theodolite and the differential GPS measurements, respectively.

4. Event Characteristics

[10] As shown by *Walter et al.* [2009], the majority of recorded seismic events show a strong Rayleigh phase preceded by small amplitude body waves, typical of surface events [*Neave and Savage*, 1970; *Deichmann et al.*, 2000; *Walter et al.*, 2008]. *Walter et al.* [2009] estimate that about 99% of the complete data set are indeed such shallow events of depth no greater than the crevasse reach (about 20 m below surface [e.g., *Paterson*, 1994]). Moreover, deeper (i.e., well below the crevasse reach) events show no surface wave, thus providing a simple criterion to separate shallow from deeper icequakes [*Walter et al.*, 2008].

[11] The Rayleigh phase is prominent on the vertical component while neither P nor S waves can be properly seen. Furthermore, Rayleigh phase waveforms are found to be highly coherent from one sensor to another in the 5–15 Hz frequency band (Figure 3). Indeed, crevassing (mode I fracturing) yields a two-lobed Rayleigh radiation pattern with maximum amplitude in the azimuth parallel to the force direction (i.e., crack opening direction) [*Gupta*, 1966]. Thus, crevassing events occurring within the array were observed with good coherency between channels (Figure 3). The frequency interval in which correlation is high corresponds to the spatial aliasing and resolution limits of a 1-D array used as

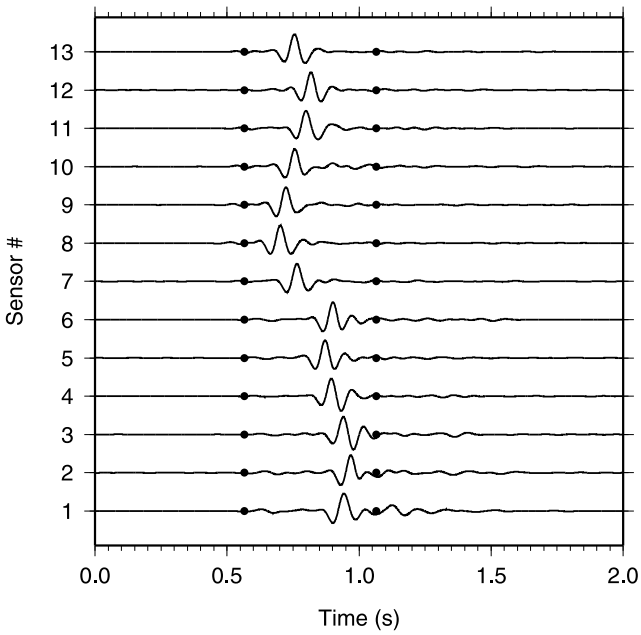

Figure 3. Plot of one event recorded by the 13 sensors used in this study, showing 5–15 Hz band-pass-filtered waveforms. The Rayleigh wave is clearly coherent. Dots denote the 0.5 s analysis window, centered on the median of the traces' maximum positions.

a first-order proxy to our network [e.g., *Gouédard et al.*, 2008], estimated using a theoretical Rayleigh wave velocity of $V = 1650$ m s^{-1} (estimated with 0.92 β [e.g., *Lay and Wallace*, 1995], where $\beta = 1790$ m s^{-1} is the S wave velocity measured by active seismics [*Gischig*, 2007]). The ice is rather homogeneous in the studied area within the corresponding wavelength range ($\lambda \in [110; 330]$ m), suggesting that incoherent pairs of seismograms on a trace-by-trace basis are most likely due to source effects rather than to path effects.

5. Locating Icequakes

[12] The waveform homogeneity mentioned in section 4 allows us to compute the time delay between pairs of sensors using cross correlation. Furthermore, as the Rayleigh phase dominates the vertical component seismograms, it is convenient to use it in order to automatically locate the ≈35000 events. However, using surface waves to locate seismic events prevents us from resolving their depth. However, we stated earlier that within the studied wavelength range ($\lambda \in [110; 330]$ m), the ice and thus the medium of propagation could be considered as an homogeneous half-space. In such a medium, Rayleigh wave's phase delay (and thus travel time) is independent of depth while its amplitude is an exponentially decaying function of depth [*Aki and Richard*, 2002]. Additionally, using a two-dimensional array necessarily yields a poor resolution on depth. Finally, and as stated earlier, about 99% of the overall activity is linked to surface processes no deeper than 20 m, i.e., at a depth an order of magnitude lower than the considered wavelength. We therefore focus on epicenters only in the remainder of this paper.

5.1. Data Preprocessing and Time Delay Calculation

[13] To compute the time delays, each velocity waveform was first filtered by a two pass, band-pass second-order Butterworth filter (equivalent to a fourth-order filter) between 5 Hz and 15 Hz. Each trace was then normalized by its peak-to-peak amplitude, and the Rayleigh phase was isolated in a 0.5 s window centered on the median position of the 13 trace maxima (see Figure 3). Time delays were then computed for each available sensor pair by time domain cross correlation. By doing so, time delays are initially multiples of the sampling rate. In order to increase the accuracy of the delay calculation, a quadratic function is fitted to the cross-correlation function using twenty samples centered on its discrete maximum. Estimating the position of the quadratic function maximum thus allows for time delay calculations with precision beyond the sampling rate (<0.001 s).

5.2. Time Delay Inversion

[14] In a homogeneous half-space, the time delays τ_{ij} between sensors i and j can be expressed as follows:

$$\tau_{ij} = \frac{1}{V}\left(\sqrt{\mathbf{X_i}^2 - \mathbf{S}^2}\right) \quad (2)$$

where $\mathbf{X_i} = (x_i, y_i)$ and $\mathbf{S} = (x_s, y_s)$ are the sensor i and source coordinates vectors, respectively, and V is the propagation velocity. Although the average velocity has been determined via active seismic experiments [*Gischig*, 2007], we consider it as an unknown in the inversion process in order to take into account possible azimuthal heterogeneities of the medium of propagation. Equation (2) relies on a circular wavefront propagation hypothesis, which is valid in the case of surface waves (where the wavefront is cylindrical); hence the poor resolution on the source depth.

[15] For each detected icequake, this therefore yields a set of N nonlinear equations in both $\mathbf{S}$ and V, where N is the number of time delays computed in the previous step. If N is larger than 3 (i.e., the number of unknowns), the problem is overdetermined and is solved using a quasi-Newton scheme [*Tarantola and Valette*, 1982, equation (25)] assuming data to have a Gaussian distribution. As the a priori information on the parameters is poorly constrained, we consider the case of an infinitely weak a priori constraint on these parameters (i.e., their variance tends to ∞), which corresponds to a classical nonlinear least squares problem [*Tarantola and Valette*, 1982]. In this case, using the notations of *Tarantola and Valette* [1982], the iterative formulation is given by

$$\mathbf{p}_{k+1} = \mathbf{p}_k + \left(\epsilon + \mathbf{G_k}^T \mathbf{C}_{\mathbf{d_0 d_0}} \mathbf{G_k}\right)^{-1} \mathbf{G_k^T} \mathbf{C}_{\mathbf{d_0 d_0}}{}^{-1} (\mathbf{d_0} - \mathbf{g}(\mathbf{p_k})) \quad (3)$$

where $\mathbf{p_k} \in \mathbb{R}^3$ is the parameter vector at iteration k (with $\mathbf{p} = (x, y, V)$), $\mathbf{d_0} \in \mathbb{R}^N$ is the data vector containing all calculated time delays, $\mathbf{G_k}$ is the $N \times 3$ matrix of partial derivatives at iteration k of the model function g (τ_{ij} from equation (2)) and $\mathbf{C}_{\mathbf{d_0 d_0}}$ is the data covariance matrix and is diagonal assuming uncorrelated time delays. The superscript ^{T} denotes the transpose operation. We introduce a regularization term ε to avoid instability during the inversion. It is empirically set to $10^{-4} \times \mathbf{I_3}$, where $\mathbf{I_3}$ is the identity matrix. Because the variance on a priori parameters tends to ∞, their expectations are chosen empirically and set to the barycenter of the array for the a priori epicenter and to 1650 m s^{-1} for the a priori velocity.

[16] Time delays calculated on waveforms that have a correlation higher than 0.80 are inverted. Standard deviation on time delays must take into account both the precision on time delay measurements and the error due to the over-simplified velocity model. They are empirically set to 0.5 ms and to 5 ms, respectively, thus yielding a total standard deviation of $\sqrt{0.005^2 + 0.0005^2} \approx 5$ ms.

[17] A posteriori uncertainties on parameters are estimated using the tangential Gaussian shape calculated around the a posteriori expectation and given by

$$\mathbf{C_{pp}} = \left(\mathbf{G^T C}_{\mathbf{d_0 d_0}} \mathbf{G}\right)^{-1} \quad (4)$$

where C_{pp} is the a posteriori covariance matrix on parameters, and G is the matrix of partial derivatives calculated at the solution. C_{pp} is diagonalized afterward to yield the final ellipsoid error.

5.3. Error Estimation

[18] In order to estimate the error due to the geometry of the array on one hand and to the time delay calculations on the other hand, we performed Monte Carlo simulations similar to those performed by *Roux et al.* [2008]. To do so, we computed theoretical time delays from each node of a 600 m × 500 m grid divided into 5 m × 5 m cells, to all seismometers. Each time delay set is then perturbed randomly 1000 times using a Gaussian distribution with a standard deviation of 1 ms and inverted using the location method previously

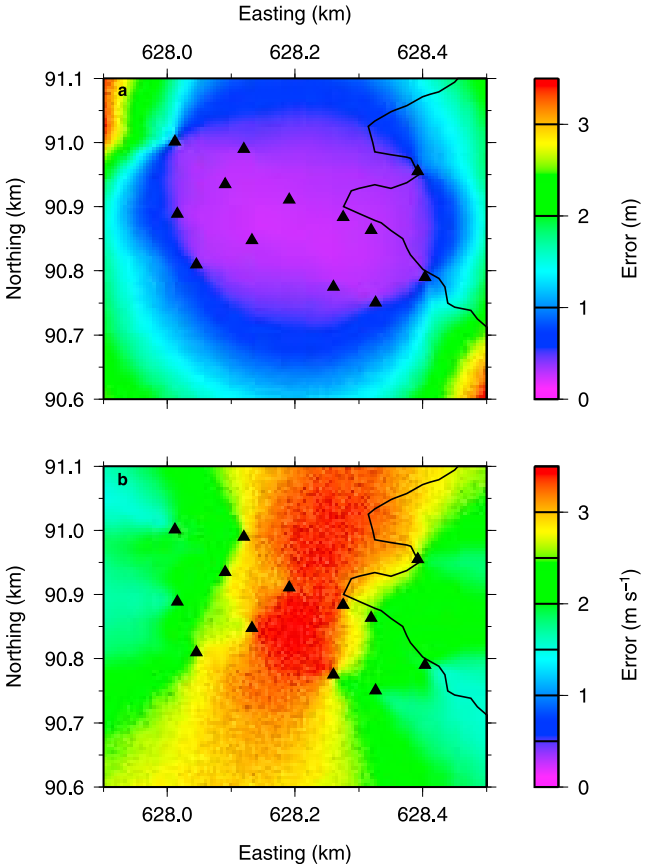

Figure 4. (a) Spatial distribution of uncertainties in epicenter location as determined by a Monte Carlo simulation. The uncertainties are low within the seismic network and increase with distance from the array. (b) Same as Figure 4a but for the velocity. Standard deviations from a mean value of 1650 m s^{-1} are shown. They remain low in the entire studied area (less than 4 m s^{-1}) and show the influence of the geometry of the array (sidelobes). Seismometers are represented as black triangles.

described. The standard deviation used in the inversion process is equal to that used with the real data (5 ms). Results of these simulations for position and velocity determination are shown in Figures 4a and 4b, respectively. Not surprisingly, the uncertainty is low within the array and increases rapidly with increasing distance from the network. Nonetheless, the standard deviation on velocity determination remains rather low within the studied area, but shows perpendicular lobes that are due to the geometry of the array.

[19] This error estimation does not take into account the over simplification of the velocity model. Indeed, we invert for the propagation velocity of the equivalent homogeneous model for each located source. This therefore yields very low error bars (of the order of 1 m) that might be unrealistic in the present context, even though (1) the velocity is allowed to vary in order to account for azimuthal heterogeneities and (2) time delays are computed for waves having a minimum wavelength of ≈110 m, which is much higher than the crevasses' width (ranging from a few centimeters [*Gischig*, 2007] to a few meters). These simulations show the spatial error pattern rather than yielding an error estimation. Given the previous considerations on inversion process and wavelength, we assumed errors of 5 to 10 m for events located within the network.

6. Results and Discussion

6.1. Spatiotemporal Evolution of Epicenters

[20] Figure 5 depicts the epicenter locations during the 17 day period prior to the outburst. Shown are locations with (1) an average standard deviation on epicenter's coordinates lower than 5 m and (2) a standard deviation on velocity lower than 50 m s^{-1}. Using these criteria, 3021 and 5499 icequakes (among 31828 located events) are selected before and after the flood initiation, respectively.

[21] Prior to the outburst, epicenters are generally oriented N–S and located at or nearby existing crevasses (Figure 5). This observation is consistent with those previously reported [*Neave and Savage*, 1970; *Helmstetter et al.*, 2001]. Figure 6 investigates in some more detail the spatiotemporal behavior of crevassing related events. Shown are epicenters located near one specific crevasse (shown in red in the inset of Figure 6a) and their time of occurrence in days relative to 1 June. Although not perfectly linear in reality, the studied crevasse is approximated by a straight line represented in red in Figure 6a. We stress that although we study one specific crevasse here, similar results were obtained for other crevasses visible in Figure 5. In the first place, we see that the events selected as occurring along the crevasse seem to be spatially random with time on long time scales (i.e., weeks), as no clear pattern appears over the entire studied period. From Figure 6b, showing the temporal evolution of epicenters projected along the red line in Figure 6a, we also see that these events tend to occur almost exclusively during daytime, when the glacier flow is more rapid. Considering the higher sensitivity of the trigger at night [*Walter et al.*, 2008], Figure 6b indicates a decrease of nocturnal activity along the crevasse that is likely to be due to the decreased longitudinal tensile stresses as there is less input of meltwater to the glacier

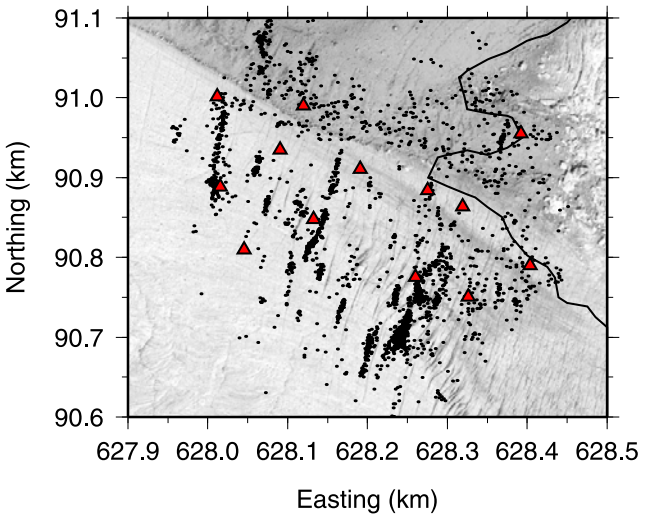

Figure 5. Locations of icequakes prior to the drainage initiation. One clearly notices the tendency that epicenters align perpendicular to ice flow, on or nearby crevasses visible in the photograph.

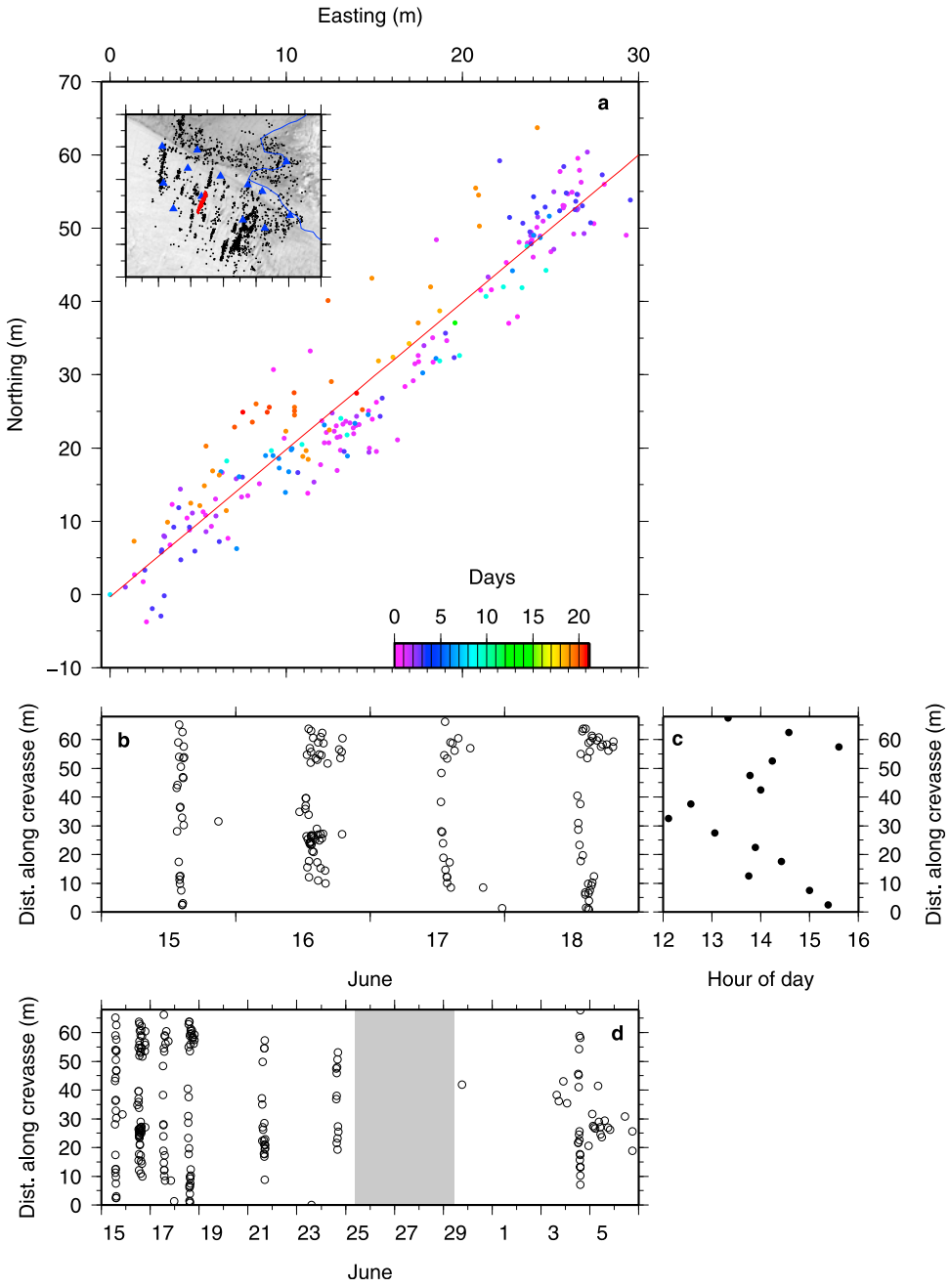

Figure 6. (a) Epicenter positions relative to the crevasse (shown by a red line and also underlined in the inset where epicenters prior to the drainage are shown) in local coordinates. The color scale represents the time elapsed since the first event located on or close to the crevasse. (b) Distance along the crevasse versus time for the first 4 days of the studied time period. (c) Distance along the crevasse versus occurrence time averaged in 5 m bins. Events occurring prior to 25 June are used in the averaging. (d) Same as Figure 6b but for the entire time period. The gray bar indicates that only recorder A (easternmost part of the array; see Figure 1) was operating.

bed at night. Furthermore, at this place, Gornergletscher merges with a tributary (Grenzgletscher; see Figure 1) in a somewhat complex manner, inducing differential sliding and thus potentially time-varying stretching of superficial ice. Figure 6c shows the occurrence time averaged in 5 m, along the crevasse distance bins. Events occurring prior to 25 June are used in the averaging process. Figure 6c suggests that icequakes tend to move on average from the center of the crevasse toward its end as time of the day increases. Thus, at smaller time scales (i.e., hours), crevassing-related icequakes seem to become spatiotemporally dependent, and cannot be considered random anymore.

[22] Figure 7 shows the epicenter locations in the 5 days following the outburst initiation with the aforementioned selection criteria. We note that, once the lake starts to drain, icequake sources are observed to shift largely toward a wide

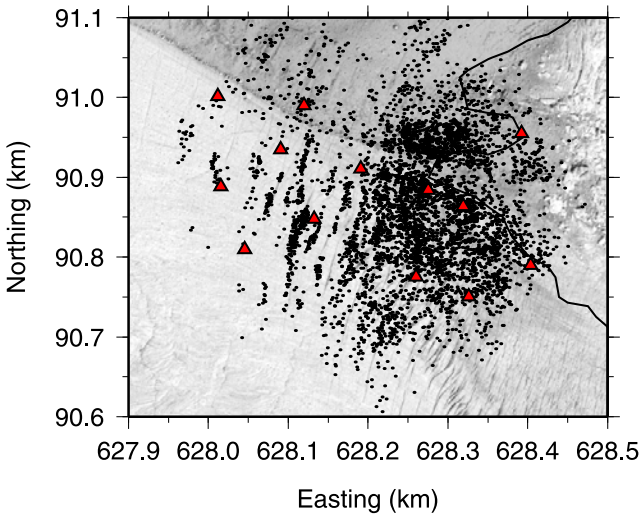

Figure 7. Locations of icequakes after the outburst started. Sources shift to a large region immediately to the west of the lake margin. Insights of the postdrainage seismic activity are given in Figure 8.

region in the eastern part of the study region (located on the western shore of the lake). Moreover, only a small proportion of events occurring after the outburst were located near crevasses in the western portion of the study region. Considering again Figure 6, we note the absence of occurrences between 25 June (day 10) and 3 July (day 17) along the studied crevasse. Although there are missing data from 25 June to 29 June due to instrument malfunctions (see *Walter et al.* [2008] for more details), it appears that there was almost no seismic activity along the crevasse from 30 June to 4 July. This feature is further visible when considering Figure 6d. This intermittence can be associated either with a lowered sensitivity of the network due to the large increase of icequakes during the outburst or with an actual decrease of seismicity in this region of the glacier. Since seismic activity along this crevasse (1) was absent during a period of relative seismic quiescence (i.e., before the outburst) and (2) reinitiated starting 4 July while the overall seismic activity was still high, we consider the latter assertion to be the more likely. Such an observation indicates that there is a significant change in stress prior to and during the outburst, thus suggesting a strong change in the overall glacier motion.

[23] Temporal evolution of postoutburst event locations is further investigated in Figure 8. Shown are 6 h time slices, except for Figure 8a showing a 24 h period. Right after the beginning of drainage, epicenters were mostly located in the vicinity of the eastern part of the seismic array, which is coincident with the western margin of the lake. We then observe a westward (i.e., in the ice flow direction) migration of the sources (Figures 8b–8g). This migration seems to cease on 4 July around noon (Figure 8h), which corresponds to the maximum of the ice dam uplift observed by *Sugiyama et al.* [2008] and described later in this study (section 6.2). Epicenters tended to form a semicircle near the lake. The highest number of icequakes was subsequently reached on 5 July at 0000 h (Figure 8j). From then on, epicenters spread again over the studied area. These observations are supported by Figure 9, which shows hourly mean easting values of epicenters. Before drainage, we observe no dynamic structure in the epicenters' average easting spread around the array's center. As previously described, the migration of epicenters can be seen after the outburst started, namely between 2 July and 4 July.

6.2. Strain Rates

[24] The surface motion near Gornersee was strongly influenced by the drainage event [*Sugiyama et al.*, 2007, 2008]. In Figure 10 we compare changes in uplift and stake distances with the seismic activity during the lake drainage. Flow changes were particularly pronounced at stakes 44 and 45 (Figure 1), which also experienced an uplift of more than 1 m, which begun around 2 July and peaked around noon on 4 July (Figure 10b). The seismic activity near the lake increased during the beginning of this uplift (Figure 10a). We also show the distances between stakes 44 and 34 in Figure 10c and between stakes 44 and 41 in Figure 10d. This approximately corresponds to the east-west and north-south directions, respectively. Near Gornersee, the ice undergoes extension in the east-west direction and compression in north-south direction under normal flow conditions. This can be attributed to the flow of Grenzgletscher which, at the confluence with Gornergletscher, changes from north to west, thus compressing the ice in the north-south direction (Figure 1). The strain pattern explains the orientation of the crevasses in the lake vicinity: the crevasses open in extensional direction, which is approximatively east to west.

[25] During the uplift period, the distance between stakes 34 and 44 temporarily decreased, whereas the distance between stakes 41 and 44 increased. This matter is elucidated further in Figure 11 where we plot the principal strains (averaged over a 6 h time period) on 1 July, 3 July and 5 July (Figures 11a, 11b and 11c, respectively). These times are indicated by the dashed vertical lines in Figure 10 and correspond to a (I) predrainage time, (II) the beginning of the uplift, and (III) the subsequent surface lowering during the drainage, respectively. We calculated principal strains from the velocity measurements at stakes 33–35 and 41–44 in a two step procedure. First, we determined a surface velocity field on a regular grid from the local measurements. At each point $\mathbf{P} = (x\ y)^T$ of the grid, we evaluated each of the velocity component $u_{j,j=1,2}$ with a surface model of the form

$$u_j = u_j^0 + a_j.x + b_j.y \tag{5}$$

where the parameters u_j^0, a_j and b_j were obtained by fitting the model to all available velocity measurements using multilinear regression. The fit was performed in a least squares sense with residuals weighted by the inverse of the distance between the grid point **P** and the respective stakes locations to the 4th power. Doing so, velocity measurements closer to the grid point under consideration are given a higher weight to measurement farther away. In a second step, the horizontal strain components at the grid points **P** were obtained from the spatial gradients of the local surface model. The strains were then converted into principal strains using standard procedure [e.g., *Turcotte and Schubert*, 2002]. The principal strains confirm the temporal evolution indicated by Figure 10. During the onset of the uplift (Figure 11b), the strain axes were rotated by nearly 90° compared to the orientation prior to the drainage (Figure 11a) and during the drainage as the

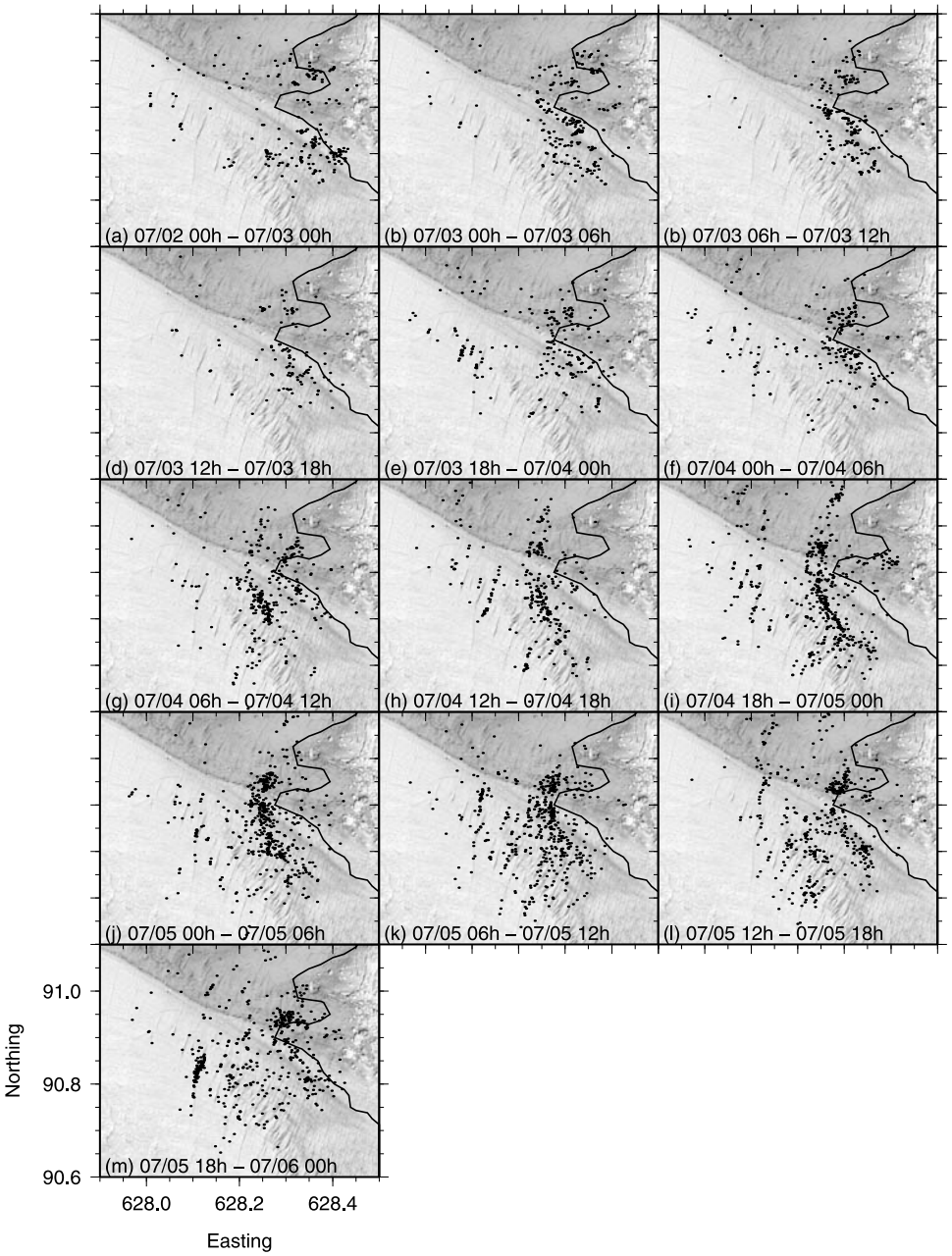

Figure 8. (a) Twenty-four hour and (b–m) six hour snapshots of icequake positions after the flood initiated. Migration and increasing number of events can clearly be seen from 2 July to 4 July. Note the semicircular shape in Figure 8i. The rate of seismic emission peaked on 5 July at 0000 h (Figure 8j).

surface lowered (Figure 11c). The magnitudes of the principal strains were highest as the surface lowered during the lake drainage, reaching values of close to 1.4×10^{-3} d^{-1} which is more than 4 times as high as before the initiation of the drainage on 1 July.

6.3. Strain Versus Location and Fault Plane Orientation

[26] Figure 11b furthermore shows that the observed increase in seismicity during the beginning of the uplift period occurred mostly on the eastern part of the seismic array. Subsequently, as the surface lowered during the lake drainage, the seismic activity increased further as the event epicenters slightly migrated toward the west (Figures 8j–8m and 9). These observations suggest that the uplift event has an effect on the occurrence and locations of near-surface icequakes, most likely by changing the surface strain rates. At this point we investigate if there is an influence of the uplift event and the concurrent changes in surface straining on the source mechanisms of near-surface icequakes. In particular, we correlate changes in fault plane orientation with the ice dam uplift. So far, we have not developed an automatic method to determine icequake source mechanisms, and therefore we confine ourselves to representative events. Most icequake activity measured on Gornergletscher consisted of tensile faulting related to the opening of surface crevasses

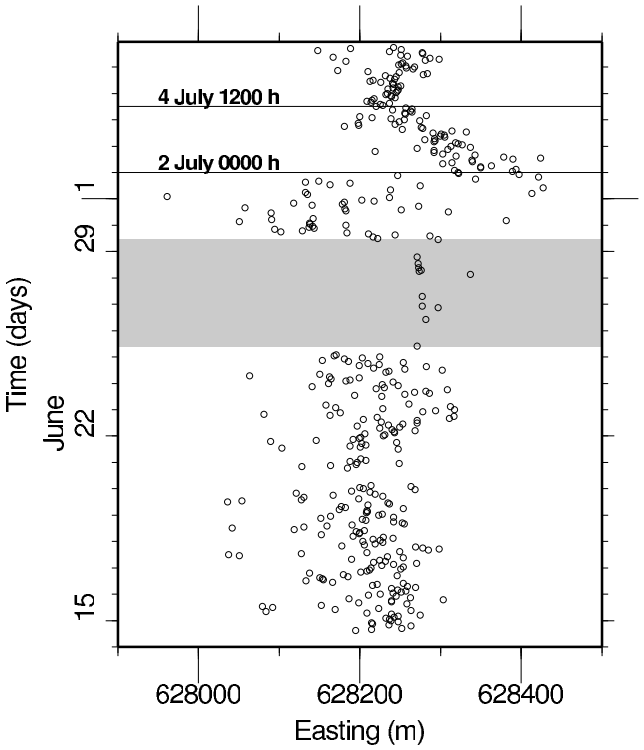

Figure 9. Plot of the evolution of 1 h averaged epicenter easting with time. Shaded zone indicates that only recorder A (easternmost part of the array; see Figure 1) was operating. From 2 July epicenters were located in the easternmost part of the network and then migrated toward the west until 4 July.

[*Walter et al.*, 2009]. Figure 1 shows that surface crevasses near the lake tend to align in the near-north-south direction. Icequake fault planes related to surface crevassing in the regular flow field are therefore expected to be nearly parallel to the north-south direction. We now concentrate on the epicenters that occurred within a small region close to stake 44 as shown in Figure 11b (red line surrounding cyan area). 95% of the over 200 events within this region occurred between 2 July and 6 July, approximately during the lake drainage. A cross-correlation analysis was performed to identify groups of events that share high waveform similarity and thus form clusters within this set of events: each event was cross correlated with all other events within the region around stake 44. An event is said to be part of a cluster if on average its maximum cross-correlation coefficient with all events of the same cluster is 0.76 or higher. The two largest clusters within the region consist of 14 and 57 events. The histograms in Figure 12 bring out the waveform similarities that distinguish these events from the rest of the events in the region around stake 44. All events of the smaller (14 events) cluster occurred on 4 July, whereas all events of the larger (57 events) cluster occurred on 2 July and 3 July. These small time windows suggest some relation to the concurrent transient change of principal strain axes orientation.

[27] To constrain the physical mechanism responsible for the events in these clusters (practically speaking, two and eleven icequakes of the smaller and larger cluster, respectively), we inverted for the (tensile crack) moment tensor using the full waveforms [*Walter et al.*, 2009]. The grid search was performed over the fault plane orientation in increments of 5° and over the moment equivalent. An example of a waveform fit with an overall variance reduction of 74% is given in Figure 13. The results show that the inverted events all have vertical fault planes and (with one exception) strike values between 80° and 100°. This means that the tensile fractures that produce the icequakes open in the north-south direction and the fault planes are oriented in the east-west direction. Due to the waveform similarities within one cluster, we suggest that the inverted events are representative of the remaining events within the specific cluster and thus conclude that these two clusters are due to tensile crack openings with fault planes parallel to the east-west direction. Such fault plane orientations strongly oppose the orientation of the main surface crevasses, which tend to align in the near-north-south direction (Figure 1). This suggests a rotation of tensile crack fault planes at the beginning of the uplift event. A plausible explanation is that the fracturing reacts to the temporary reorientation of principal strain axes at the beginning of the uplift event.

6.4. Overview of Seismic Response to Lake Drainage

[28] In terms of near-surface seismicity and deformation, the outburst can be decomposed into three major episodes that summarize our observations.

[29] 1. The overall seismic activity started increasing on 2 July. As can be seen from Figure 7, most epicenters in this period were located near the lake in the eastern part of the array. The epicenters no longer tended to align along crevasses as was the case during the previous two weeks.

[30] 2. A first peak in seismic activity was reached on 3 July (see Figure 10a). The epicenters started to migrate toward the west (see Figures 8b–8e)). During this time, principal strain axes rotated by nearly 90° (Figure 11): the compressional axis was then oriented in the flow direction (east-west) rather than perpendicular to it. Moment tensor solutions of icequake clusters (Figure 13) show fault plane rotations in accordance with the rotation of the principal strain axes.

[31] 3. The uplift at stake 44 reached its maximum around noon on 4 July. The seismic activity peaked again at night and epicenters tended to align along a semicircle (Figures 11c and 8f–8i). Seismic events again showed a tendency to linearly align along surface crevasses (Figure 6). Principal strain axes had rotated back to their original orientation, but their respective amplitudes were higher than prior to the lake drainage (Figure 11).

[32] On the basis of these observations, we propose the following mechanisms to explain the spatiotemporal evolution of the seismic activity. *Sugiyama et al.* [2007, 2008] pointed out an important modification of the horizontal motion of the ice dam: stakes 44 and 45 (located near the lake shore; see Figure 1) experienced either a 90° or a 180° shift in their direction of displacement, respectively, when the drainage started on 2 July (Figure 14). The motion returned to its initial direction at the time of the uplift maximum on 4 July. This behavior strongly suggests that the ice dam was decoupled from its bedrock between 2 July and 4 July. In addition, the aforementioned calving event (Part 2) at the very beginning of the outburst also suggests the (partial) breaking of the ice dam away from the rest of the glacier: as the dam floated up, it fractured pervasively. Although it remained in

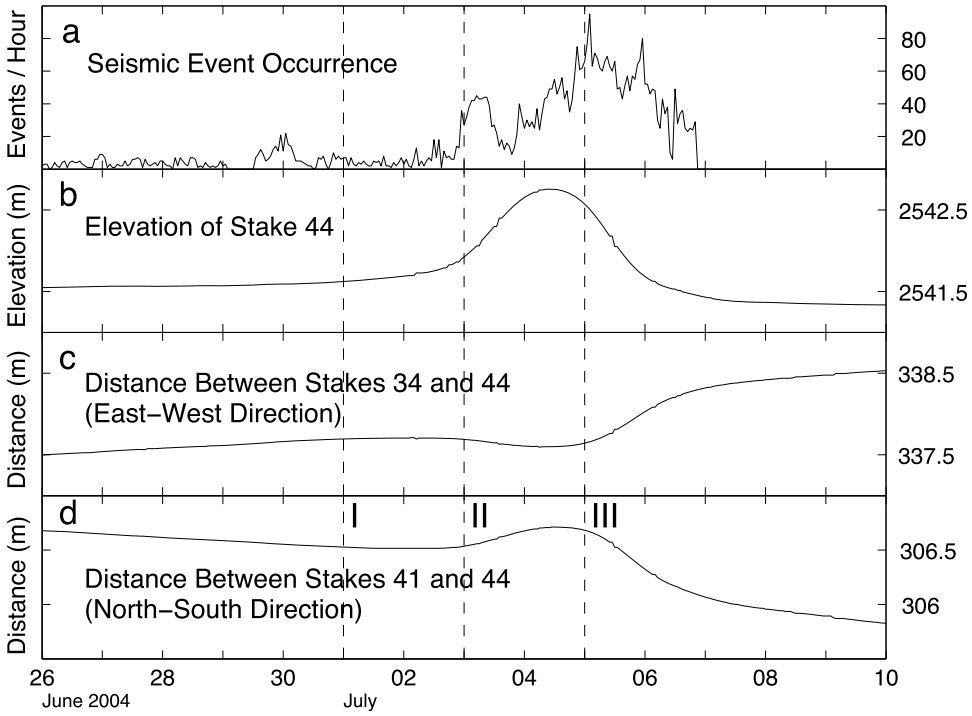

Figure 10. Temporal evolution of seismic activity (using located events only) and surface deformation in the region of the seismic network. (a) The seismic activity increases with (b) the uplift of stake 44. This event also interrupts (c) the overall extension in east-west direction and (d) the overall compression in north-south direction. Dashed vertical lines indicate times for which principal strains are shown in Figure 11.

contact with the rest of the glacier, there was severe damage between the ice dam and the grounded ice. It is thus very likely that the uplift process is not only viscous, but also brittle. Thus, as soon as the drainage started, gravity pushed the now floating and detached ice dam into the western grounded ice as the glacier bed dropped strongly toward the west. This contributed to temporarily changing the stress field within the ice dam from longitudinal extension to longitudinal compression, i.e., compression along the east-west direction. The "diffusely" ordered epicenters in the eastern part of the seismic network accompany the uplift of the ice dam, because the basal water causing the uplift may not have entered the ice-bedrock interface uniformly. When the ice dam lowered and recoupled to the glacier bed, tensile

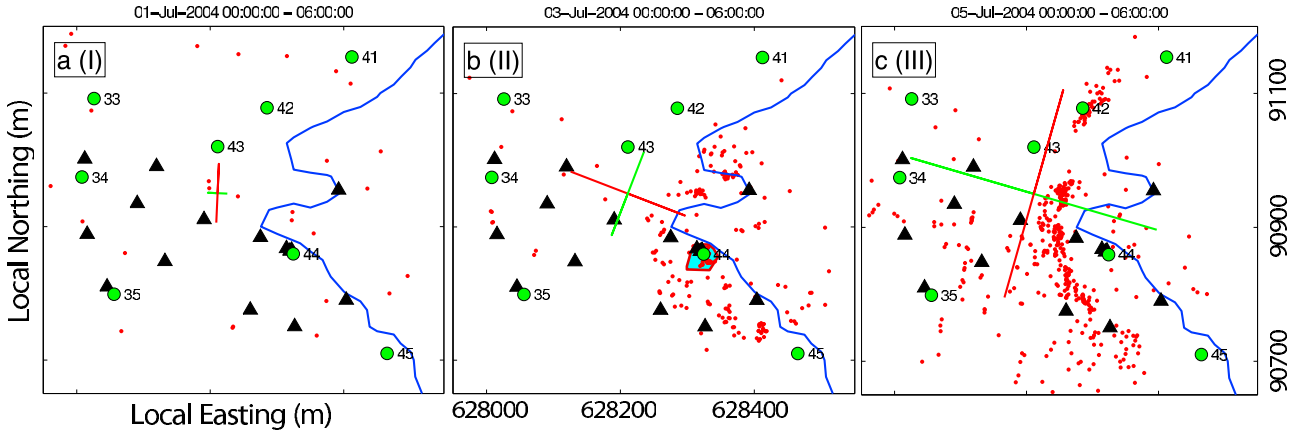

Figure 11. (a–c) Principal strains in the region of the seismic array (black triangles) during the three 6 h periods indicated in Figure 10. The green crossbars indicate extensional strains, and the red crossbars indicate compressional strains. Red dots represent epicenters of seismic events that occurred within this time period. The blue line shows the outline of Gornersee at its maximum level in 2004, and the green dots mark stakes used to measure surface motion. In Figure 11b the seismicity around stake 44 scrutinized in some detail as described in the text is shown by the cyan area (surrounded in dark red). Note that in Figure 11b the strain axes are rotated by almost 90° with respect to the plots.

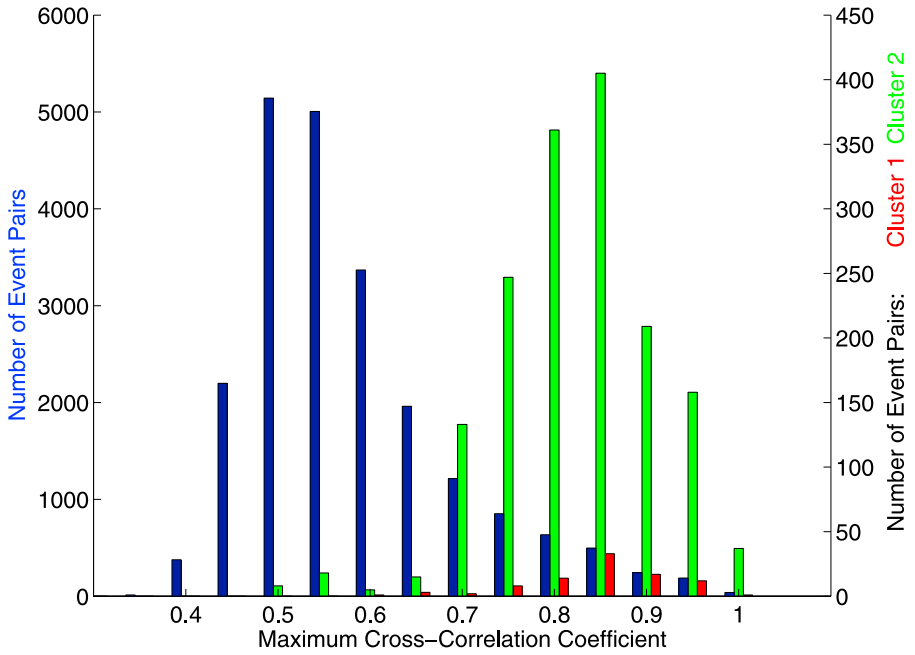

Figure 12. Histograms of maximum cross-correlation coefficients between all event pairs of three groups: first (blue bars), all events occurring within the region close to stake 44 (indicated by the cyan area in Figure 11b), second (red bars), all events of the smaller cluster in this region, and third (green bars), all events of the larger cluster in this region. The histograms clearly show that events within either one of the clusters are distinguished from the remainder of the events near stake 44 by having greater waveform similarities.

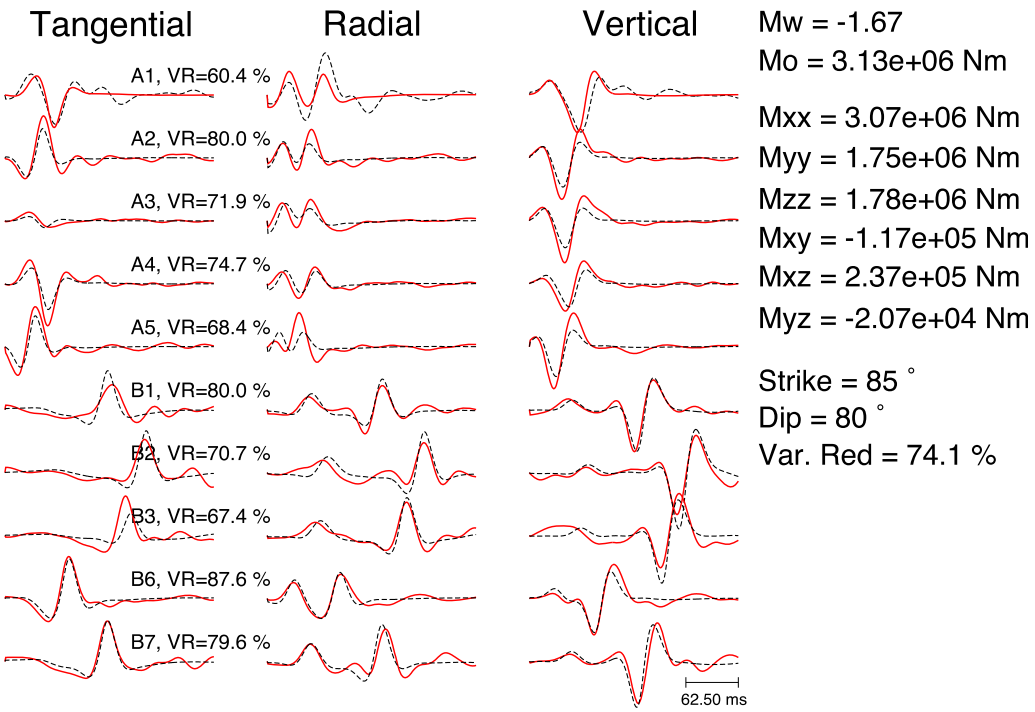

Figure 13. Three-component (tangential, radial, and vertical in source-receiver coordinates) waveform fit of one surface icequake from the larger cluster (see text for details) using the tensile crack moment tensor inversion. Green's functions for a homogeneous half-space were used, and waveforms were filtered between 5 and 30 Hz. Red solid and black dashed lines represent data and synthetic seismograms, respectively. Variance reductions for individual stations are indicated. The dominant Rayleigh phases and S phases are well reproduced at an overall variance reduction of 0.74.

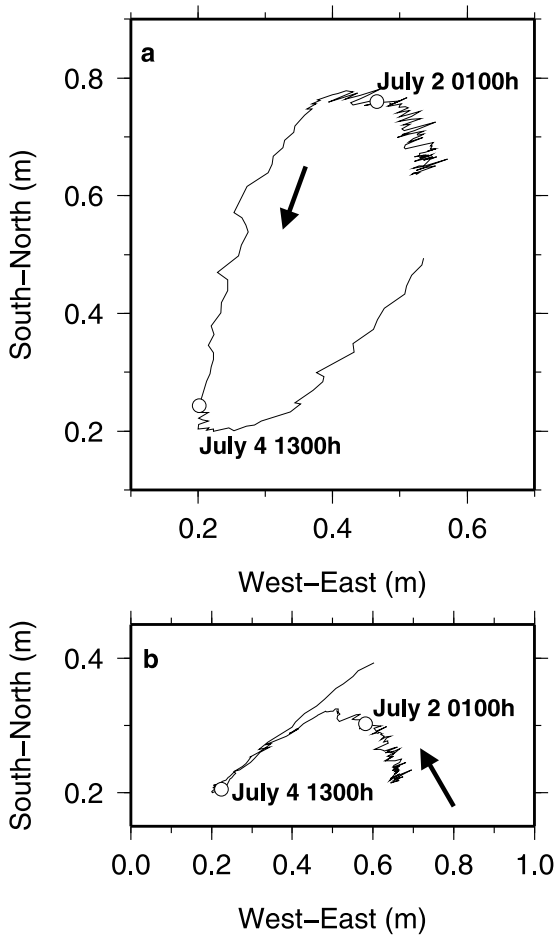

Figure 14. Plan view of the stake motion at stakes (a) 45 and (b) 44. Arrows indicate the general direction for each stake. Time stamps are also shown by open circles. Modified from *Sugiyama et al.* [2008].

extension within the ice dam resumed in the east-west direction. At this point the strain rates were substantially higher than before the drainage initiation (Figure 11) because of a weaker bed beneath the ice dam.

[33] Crevassing behavior prior and during the outburst further suggest the detachment of the ice dam from the rest of the glacier. As the former was afloat it moved westward and compressed the latter where the crevasse studied in section 6.1 (Figure 6) was located, thus inhibiting tensile extension within the still grounded ice. Crevassing in the western part of the study area resumed on 4 July when the ice dam recoupled to the glacier bed (Figure 6b).

7. Conclusions

[34] In order to investigate the influence of an outburst flood of a glacier-dammed lake at Gornergletscher on the surface microseismic activity (so-called "icequakes"), we designed an automated location procedure that inverts time delays computed on surface waves with a quasi-Newton scheme. We showed that the uplift of a portion of the glacier generated a compressed zone with strain axes parallel to the glacier flow (i.e., perpendicular to what is usually seen). During the outburst event, the normal/dominant mode of seismic activity associated with tensile surface crevassing was inhibited at some parts of the glacier. We proposed that (at least part of) the ice dam was actually detached from the rest of the glacier and flowing westward into the still grounded ice. This interpretation explains both the rotation of principal stress axes within the dam and the inhibition of tensile surface crevassing in the grounded ice. It is also consistent with previous results inferring the existence of a hinge [*Sugiyama et al.*, 2008] acting as a boundary between floating and grounded ice. We furthermore showed that crevassing at Gornergletscher occurred mostly during daytime, with a migration from center to both ends of the crevasse. Interestingly, this behavior is no longer valid on longer time scales (of the order of several days) as events seem to occur randomly in both time and space along the crevasse.

[35] **Acknowledgments.** The authors would like to thank B. Valette for his help on the inverse problem resolution. D. Marsan is acknowledged for comments on the first version of this paper. Invaluable comments from three anonymous referees, Martin Truffer, and Michael Church all contributed to significantly enhance the quality of the manuscript. The project was funded by the Swiss National Science Foundation grant 200021-103882/1. P.-F.R. was supported by the Conseil Général de la Région Rhône-Alpes. Some figures were made using the GMT package [*Wessel and Smith*, 1991].

References

Aki, K., and P. G. Richard (2002), *Quantitative Seismology*, 2nd ed., Univ. Sci. Books, Sausalito, Calif.

Allen, R. (1978), Automatic earthquake recognition and timing from single traces, *Bull. Seismol. Soc. Am.*, *68*(5), 1521–1532.

Björnsson, H. (1998), Hydrological characteristics of the drainage system beneath a surging glacier, *Nature*, *395*(6704), 771–774, doi:10.1038/27384.

Danesi, S., S. Bannister, and A. Morelli (2007), Repeating earthquakes from rupture of an asperity under an Antarctic outlet glacier, *Earth Planet. Sci. Lett.*, *253*, 151–158.

Deichmann, N., J. Ansorge, F. Scherbaum, A. Aschwanden, F. Bernardi, and G. H. Gudmundsson (2000), Evidence for deep icequakes in an Alpine glacier, *Ann. Glaciol.*, *31*(1), 85–90.

Gischig, V. (2007), Seismic investigations on Gornergletscher, Master's thesis, Inst. of Geophys., ETH Zurich, Zurich, Switzerland.

Gouédard, P., C. Cornou, and P. Roux (2008), Phase-velocity dispersion curves and small-scale geophysics using noise correlation slantstack technique, *Geophys. J. Int.*, *172*, 971–981.

Gupta, I. (1966), Use of reciprocity theorem for obtaining Rayleigh wave radiation patterns, *Bull. Seismol. Soc. Am.*, *56*(4), 925–936.

Helmstetter, A., J.-R. Grasso, B. Hernandez, M. Bouchon, M. Dietrich, and the Girose team (2001), Mechanics of icequakes (La Girose glacier, French Alps), paper presented at 26th General Assembly, Eur. Geophys. Soc., Nice, France, 26–30 March.

Huss, M., A. Bauder, M. Werder, M. Funk, and R. Hock (2007), Glacier-dammed lake outburst events of Gornersee, Switzerland, *J. Glaciol.*, *53*(181), 189–200.

Lay, T., and T. Wallace (1995), *Modern Global Seismology*, *Int. Geophys. Ser.*, vol. 58, 1st ed., 521 pp., Academic, San Diego, Calif.

Neave, K. G., and J. C. Savage (1970), Icequakes on the Athabasca Glacier, *J. Geophys. Res.*, *75*, 1351–1362.

Paterson, W. (1994), *The Physics of Glaciers*, 3rd ed., Pergamon, New York.

Raymond, M., M. Wegmann, and M. Funk (2003), Inventar gefährlicher Gletscher in der Schweiz, *Tech. Rep. 182*, ETH Zurich, Zurich, Switzerland.

Roberts, M. J. (2005), Jökulhlaups: A reassessment of floodwater flow through glaciers, *Rev. Geophys.*, *43*, RG1002, doi:10.1029/2003RG000147.

Roux, P.-F., D. Marsan, J.-P. Métaxian, G. O'Brien, and L. Moreau (2008), Micro-seismic activity within a serac zone in an Alpine glacier (Glacier d'Argentière, Mont-Blanc, France), *J. Glaciol.*, *54*(184), 157–168.

St. Lawrence, W., and A. Qamar (1979), Hydraulic transients: A seismic source in volcanoes and glaciers, *Science*, *203*(4381), 654–656.

Sugiyama, S., A. Bauder, P. Weiss, and M. Funk (2007), Reversal of ice motion during the outburst of a glacier-dammed lake on Gornergletscher, Switzerland, *J. Glaciol.*, *53*(181), 172–180.

Sugiyama, S., A. Bauder, M. Huss, P. Riesen, and M. Funk (2008), Triggering and drainage mechanisms of the 2004 glacier-dammed lake outburst in Gornergletscher, Switzerland, *J. Geophys. Res.*, *113*, F04019, doi:10.1029/2007JF000920.

Tarantola, A., and B. Valette (1982), Generalized nonlinear inverse problems solved using the least squares criterion, *Rev. Geophys.*, *20*, 219–232.

Turcotte, D. L., and G. Schubert (2002), *Geodynamics*, 2nd ed., Cambridge Univ. Press, Cambridge, U. K.

Walter, F., N. Deichmann, and M. Funk (2008), Basal icequakes during changing subglacial water pressures beneath Gornergletscher, Switzerland, *J. Glaciol.*, *54*(186), 511–521.

Walter, F., J. F. Clinton, N. Deichmann, D. S. Dreger, S. E. Minson, and M. Funk (2009), Moment tensor inversions of icequakes on Gornergletscher, Switzerland, *Bull. Seismol. Soc. Am.*, *99*(2A), 852–870, doi:10.1785/0120080110.

Wessel, P., and W. H. F. Smith (1991), Free software helps map and display data, *Eos Trans. AGU*, *72*(41), 441.

M. Funk, P. Riesen, and F. Walter, Versuchsanstalt für Wasserbau, Hydrologie und Glaziologie, ETH Zurich, CH-8092 Zürich, Switzerland. (funk@vaw.baug.ethz.ch; riesen@vaw.baug.ethz.ch; fwalter@vaw.baug.ethz.ch)

P.-F. Roux, Laboratoire de Géophysique Interne et Tectonophysique, Université de Savoie, CNRS, Campus Scientifique, F-73376 Le Bourget-du-Lac CEDEX, France. (pierre-francois.roux@obs.ujf-grenoble.fr)

S. Sugiyama, Institute of Low Temperature Science, Hokkaido University, Sapporo 060-0819, Japan. (sugishin@lowtem.hokudai.ac.jp)